

Investigation of Space Charge Effects in Magnetized Electron Beam

W.M.Sajini Wijethunga
Center for Accelerator Science
Old Dominion University, Norfolk, VA

February 28, 2019

Contents

1	Introduction	3
2	Space charge effect	4
2.1	Space charge forces	4
2.2	Space charge current limitation	5
3	Emittance compensation in a magnetization and space charge dominated beam	6
4	Experimental setup	7
5	Measurements	9
6	Results and Discussion	9
7	Simulations	11
8	Summary	12

1 Introduction

The proposed Jefferson Lab Electron-Ion Collider (JLEIC) is required to deliver a ultra-high luminosity, exceeding $10^{33} \text{ cm}^{-2}\text{s}^{-1}$ to examine the hadronic structure of matter. According to the following equation

$$L = \frac{1}{4\pi} f_0 N_b \frac{N_e N_p}{\sigma_x \sigma_y}, \quad (1)$$

(where N_e , N_p and σ_x , σ_y represent the number of particles per bunch and beam sizes of the two colliding beams respectively, frequency f and number of bunches N_b)[1],

high luminosity can be achieved with high bunch charge and small beam sizes (small transverse emittance) of both colliding electron and ion beams together with high bunch repetition rate. In order to obtain this small transverse emittance (less momentum spread in the ion beam) electron cooling is used.

Electron cooling was invented by G.I. Budker in 1965 for the purpose of increasing luminosity of hadron collider. The idea behind this is when an electron beam with temperature T_e is co-propagated with the ion beam with temperature T_i where $T_e < T_i$ and same velocity, Coulomb collisions between ions and electrons lead to a transfer of thermal energy from ions to the electrons. Thermal equilibrium is reached when both the particles have the same transverse momentum. Hence, the lighter electrons get higher transverse velocities by slowing down the heavy ions, which reduces the transverse emittance [2].

In order to have an efficient cooling, the cooling electron beam should have high bunch charge, high repetition rate, low temperature (low emittance and low energy spread), and large enough transverse beam size to cool the traversing ion beams. However, these features can combine in enhancing the collective interaction, such as space charge effect.

In 1977, Y.Derbenev discovered a way to increase the cooling efficiency by using a "magnetized electron beam", where the cooling process occurs inside a uniform longitudinal magnetic field [3, 4]. Here, the electrons follow small helical trajectories, which work in favor of increasing the electron-ion interaction time and thereby improving the cooling efficiency. In addition, the cyclotron motion also provides suppression of electron-ion recombination.

One challenge associated with implementing the cooling process inside a magnetic field is the radial fringe field at the entrance or exit of this cooling solenoid. This field exerts an azimuthal kick on the electrons that produces a rotational motion. This motion has a very large radius and a very large resultant emittance. As a solution to this problem, the electron beam can be generated inside a magnetic field that cancels the kick at the entrance of the cooling solenoid by an earlier kick at the exit of the cathode solenoid.

Following diagram shows the transportation of the magnetized electron beam from its generation to the cooling solenoid.

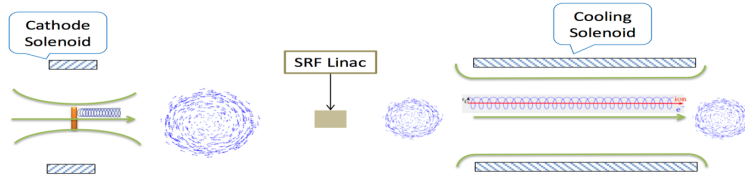


Figure 1: Illustration of the beamline from generation of the magnetized beam to the cooling solenoid

According to the Busch's theorem, the conservation of the canonical angular momentum of a

charged particle moving in an axially symmetric magnetic field can be explained by,

$$\mathcal{L} = \gamma m r^2 \dot{\phi} + \frac{1}{2} e B_z r^2, \quad (2)$$

where γ is the Lorentz factor, $\dot{\phi}$ the time derivative of ϕ , and m and e are the electron rest mass and charge respectively. The average canonical angular momentum of the electrons \mathcal{L} is obtained by averaging Eq. (2) over the beam distribution. At the photocathode, we have $\dot{\phi}=0$ and

$$\langle \mathcal{L} \rangle = \frac{1}{2} e B_z r^2 = e B_0 \sigma_c^2, \quad (3)$$

where $B_0 = B_z(z = 0)$ is the axial magnetic field at the photocathode and σ_c is the transverse root-mean-square (rms) beam size at the photocathode in Cartesian coordinates.

Outside the solenoidal field region where $B_z(z) = 0$, the second term of Eq. (2) vanishes and the canonical angular momentum is given by the first term of Eq. (2), which is the axial mechanical angular momentum [5, 6].

$$\mathcal{L} = \gamma m r^2 \dot{\phi}, \quad (4)$$

As a preliminary step towards the JLEIC electron cooler, we have successfully generated the magnetized electron beam at JLab Gun Test Stand(GTS) using a compact 300 kV DC high voltage photogun with an inverted insulator geometry and alkali-antimonide photocathode. Furthermore, characterization of the magnetized beam have been done by measuring the beam size variations, rotation angle variations and emittance variations with the magnetic strength [7]. However, in this work I'm going to focus on the space charge effect in the magnetized electron beam specifically, whether the magnetization affect the space charge current limitation near the photocathode.

2 Space charge effect

2.1 Space charge forces

Space charge is a accumulation of charges in a particular region which are emitted from the metal surface. The Coulomb repulsive forces inside this charge accumulation are called the space charge forces. These space charge forces in high intensity accelerators/colliders can degrade the beam quality and cause instabilities as a result of beam emittance growth, energy spread, halo formation, particle losses and even can set up an upper limit for the beam current.

Let's derive the equation for the direct space charge forces in free space. In a uniform cylindrical charge distribution with radius a and longitudinal charge distribution $\lambda(r) = \lambda_0(r/a)^2$ travelling with a relativistic constant velocity $v = \beta c$, the electric and magnetic fields can be computed as below.

Applying Gauss's law,

$$E_r(2\pi r)\Delta z = \frac{\lambda(r)\Delta z}{\epsilon_0} \rightarrow E_r = \frac{\lambda_0}{2\pi\epsilon_0} \frac{r}{a^2} \quad (5)$$

Applying Ampere's law,

$$B_\phi(2\pi r) = \mu_0 I = \mu_0 \beta c \lambda(r) \rightarrow B_\phi = \frac{\lambda_0 \beta}{2\pi\epsilon_0 c} \frac{r}{a^2} = \frac{\beta}{c} E_r \quad (6)$$

Thus, the electromagnetic transverse force acting on a charge inside the beam is given by the Lorentz force $\vec{F} = q(\vec{E} + \vec{v} \times \vec{B})$,

$$F_r(r) = q(E_r - \beta c B_\phi) = q E_r (1 - \beta^2) = \frac{q}{\gamma^2} \frac{\lambda_0}{2\pi\epsilon_0} \frac{r}{a^2} \quad (7)$$

As per the above equation, the electric force is defocusing the beam and the magnetic force is focusing the beam. For relativistic particles, the magnetic force almost balances the electric force. But for non-relativistic particles (low-energy beams, near the cathode), the magnetic force is negligible and the beam spreads rapidly due to the defocusing. Also, this transverse space charge force is inversely proportional to the bunch dimensions [8].

We can apply this to Gaussian charge distribution. The charge density can be written as,

$$\rho(r, z) = \frac{q_0}{(\sqrt{2\pi})^3 \sigma_z \sigma_r^2} e^{(-z^2/2\sigma_z^2)} e^{(-r^2/2\sigma_r^2)}, \quad (8)$$

where q_0 is the bunch charge σ_z and σ_r are longitudinal and transverse rms beam sizes. Hence, applying the Gauss's law,

$$E(r, z) = \frac{1}{2\pi\epsilon_0} \frac{q_0}{\sqrt{2\pi}\sigma_z\sigma_r^2 r} e^{(-z^2/2\sigma_z^2)} \int_0^r e^{(-r'^2/2\sigma_r^2)} r' dr' \quad (9)$$

$$E(r, z) = \frac{1}{2\pi\epsilon_0} \frac{q_0}{\sqrt{2\pi}\sigma_z} e^{(-z^2/2\sigma_z^2)} \left[\frac{1 - e^{(-r^2/2\sigma_r^2)}}{r} \right] \quad (10)$$

The total force inside the bunch can be written as,

$$F_r(r, z) = qE_r(1 - \beta^2) = \frac{q}{2\pi\epsilon_0\gamma^2} \frac{q_0}{\sqrt{2\pi}\sigma_z} e^{(-z^2/2\sigma_z^2)} \left[\frac{1 - e^{(-r^2/2\sigma_r^2)}}{r} \right] \quad (11)$$

2.2 Space charge current limitation

When space charge accumulates and forms a cloud of charges next to the cathode it limits further emission of charges from the surface due to the space charge forces. This is known as the space charge current limitation.

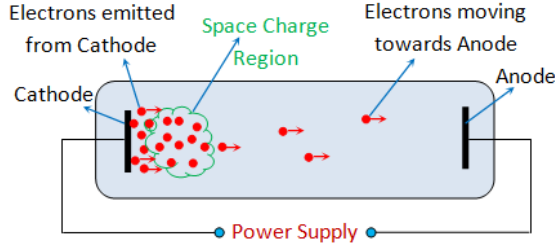


Figure 2: Illustration of the space charge current limitation

Child and Langmuir first studied the maximum current density J that can be transported from an infinite planar cathode at zero potential to an infinite planar anode parallel to the cathode at a distance d and fixed potential difference V when the initial velocity of electrons at the cathode is zero, due to the space charge limitations, by solving the 1D Poisson's equation with the continuity equations and equation of motion [5, 9],

$$J = \frac{4\epsilon_0}{9d^2} \sqrt{\frac{2e}{m}} V^{3/2} \quad (12)$$

Thus, the current can be increased by either increasing the voltage or decreasing the cathode

anode spacing. Since in practical situations these conditions are not the same such as the finite planes, non zero initial velocity, varying potential difference, above equations can use as a useful approximation for the maximum current density.

The charge saturation (current limitation) at the photocathode can be explained by combining the space charge effect and Fowler-Nordheim limit, which gives the maximum current density extracted from a surface under a given electric field, by treating the emission of electrons from a metal-vacuum interface, in the presence of an electric field normal to the surface, as a quantum mechanical tunneling process.

$$J(s) = \frac{AE(s)^2}{\phi_w t^2(y)} \exp \left[\frac{-Bv(y)\phi_w^{3/2}}{E(s)} \right], \quad (13)$$

and $y = (eE(s)/4\pi\epsilon)^{(1/2)}/\phi_w$ where $E(s)$ is the normal component of electric field at cathode surface, ϕ_w is the work function of the metal, A and B are constants, and $v(y)$ and $t(y)$ represent the effect due to image charge effects (image charges can be defined as the fields of the bunch including the (cathode) boundary condition minus the fields of the bunch in free space) [10].

Space charge accumulate at the cathode suppresses the surface field and thus, following the reduced surface field, less particles will be injected according to Fowler-Nordheim equation. When the electric field from the emitted charge balances the surface charge, saturation occurs.

3 Emittance compensation in a magnetization and space charge dominated beam

The paraxial envelope equation with space charge fields is given by following equation.

$$r_m'' + \frac{\gamma'}{\gamma\beta^2} r_m' + \frac{\gamma''}{2\gamma\beta^2} r_m + \left(\frac{qB}{2mc\beta\gamma}\right)^2 r_m - \left(\frac{p_\theta}{mc\gamma\beta}\right)^2 \frac{1}{r_m^3} - \left(\frac{\epsilon_n}{\beta\gamma}\right)^2 \frac{1}{r_m^3} - \frac{K}{r_m} = 0, \quad (14)$$

where r_m is the beam radius, B is the solenoid field, $p_\theta = \gamma m r^2 \dot{\phi} + \frac{1}{2} e B_z r^2$ is the canonical angular momentum of the particles as determined by the initial conditions, $\epsilon_n = \beta\gamma\epsilon$ is the normalized emittance and $K = \frac{I}{I_0} \frac{2}{\beta^3\gamma^3}$ is the generalized perveance, which indicates how significant the space charge effect is on the beam's motion and I is the beam current and $I_0 = \frac{4\pi\epsilon_0 mc^3}{q} \approx \frac{1}{30} \frac{mc^2}{q} \approx 17$ kA for electron is the characteristic current [5].

The first term, r_m'' , represents the change of slope of the particle trajectory. The second term contains the effect of the axial electric field (acceleration or deceleration), the third term that of the radial electric field (focusing, defocusing), and the fourth term represents the magnetic force. The fifth term represents a centrifugal potential or an effective repulsive core when the canonical angular momentum is finite. The last two terms are added to the general paraxial envelope equation by considering the space charge fields on a beam propagating inside a drift tube. Thus the sixth term represents the emittance variations and the last term represents the space charge effect. When $B \neq 0$ at the cathode, then from Busch's theorem (3), $p_\theta = \frac{1}{2} e B_z r^2$ where B_z and r are the longitudinal magnetic field and the beam radius at the cathode respectively.

According to the above equation, the emittance term has the same $\frac{1}{r^3}$ dependence as the angular momentum term, which are repulsive forces tending to diverge the beam. If we equate the two terms,

$$\left(\frac{p_\theta}{mc\gamma\beta}\right)^2 \frac{1}{r_m^3} = \left(\frac{\epsilon_n}{\beta\gamma}\right)^2 \frac{1}{r_m^3} \quad (15)$$

$$\frac{p_\theta}{mc} = \epsilon_n = \gamma\beta\epsilon \quad (16)$$

Also the emittance due to magnetization can be written as,

$$\epsilon_n = \epsilon_d = \frac{eB_z r^2}{2mc}, \quad (17)$$

which called as the drift emittance or magnetized emittance.

Thus, a nonzero canonical angular momentum, which gives rise to a rotation of the particle trajectories and hence a centrifugal force, has the same effect as the normalized emittance. Applying this idea to our experiment, the magnetic field at the cathode can generate canonical angular momentum, which in effect increases the normalized emittance of the electron beam. The larger drift emittance results in larger transverse beam size, which is inversely proportional to the space charge forces [5, 11]. However, this drift emittance is apply only to the normal beam transportation region, not inside the solenoids. In this experiment we are investigating whether there is any effect like this at the cathode such that it'll help to decrease the space charge current limitations.

4 Experimental setup

The experimented beam line consists mainly of a with bialkali antimonide (K_2CsSb) photocathode, DC gun high voltage chamber, cathode solenoid, laser, focusing solenoids, correctors and diagnostics equipment such as YAG screens and harp.

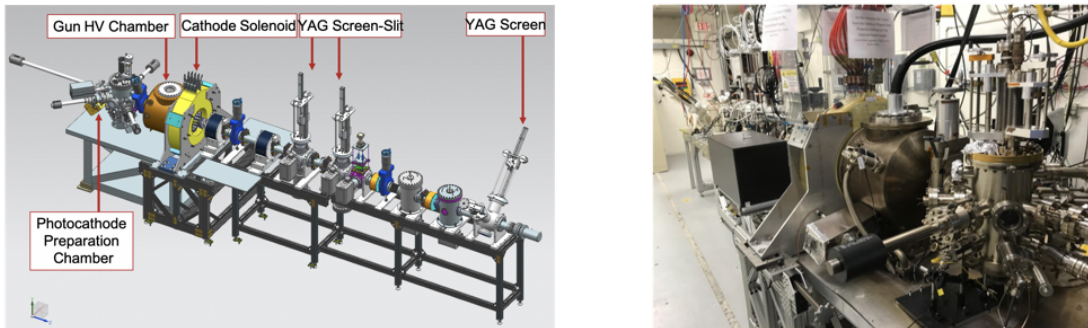


Figure 3: Experimental setup

In preparation of the photocathodes, a load-lock type photocathode deposition chamber was installed behind the gun high voltage chamber where pure elemental sources of Sb, Cs, and K are thermally evaporated and deposited onto two different substrate materials, GaAs and molybdenum, with various thickness of the Sb layers by changing the deposition time. For this experiment, the photocathode was made from a GaAs substrate with 90 min deposition time of Sb layer and molybdenum substrate with 10 min deposition time of Sb layer were used. Both showed quantum efficiency (QE), which is the ratio of number of emitted electrons to the incident photons, in the range of 5-8% with the 515 nm green laser. The photocathode active area was limited to a 3 mm radius, where the full substrate radius is 6.5 mm, in order to reduce beam halo, vacuum excursions, and high voltage arcing, and to increase the photocathode lifetime.

For this experiment, we used high energy femtosecond fiber laser with 515 nm wavelength, 500 fs pulse width and 40μJ pulse energy, operating up to 50 kHz repetition rate. The laser temporal

profile was Gaussian. The laser size at the photocathode was adjusted and the pulse width was stretched to get few different values by using an optical transport system with focusing lenses and diffraction grating.

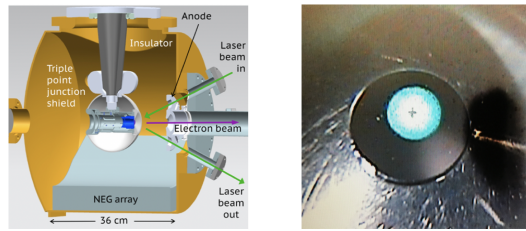


Figure 4: Laser path (left). Gaussian laser spot on the cathode (right).

A compact DC high voltage photogun with an inverted insulator and spherical cathode electrode with a screening shed was designed and installed at GTS for the project. The gun was initially operated at 350 kV but by the time we got the measurements it was operated at maximum 225 kV due to some field emission effects. Fig:5 shows the electric field map of the gun.

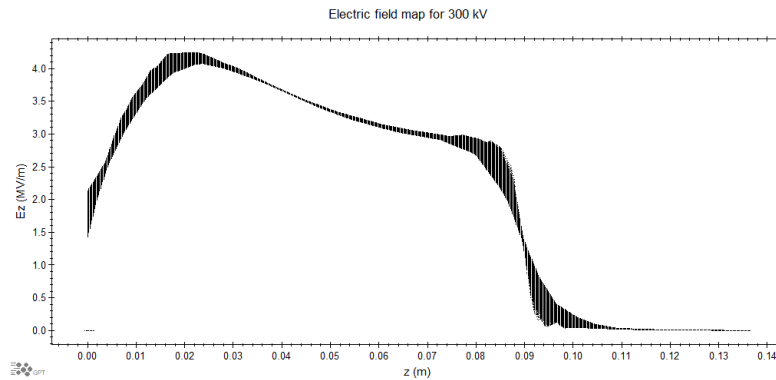


Figure 5: Gun field map for 300 kV.

The magnetic field at the photocathode is provided by the solenoid magnet, which was designed to fit at the front of the gun chamber 0.2 m away from the cathode.

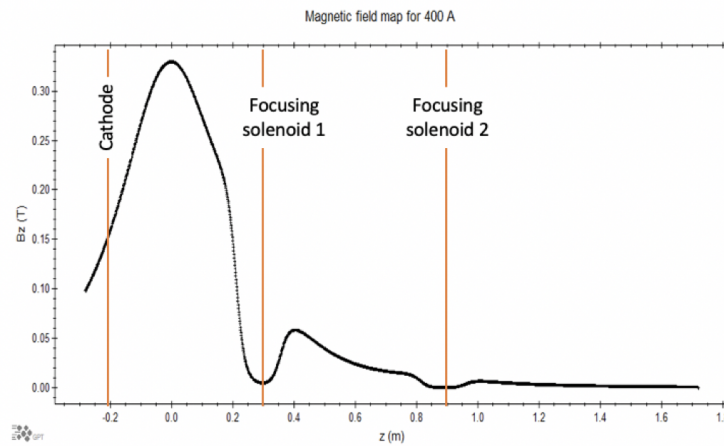


Figure 6: Solenoid field map for 400 A.

The solenoid dimensions are 11.8'' ID, 27.6'' OD, and 6.2'' width, comprised of 16 layers of 20

turn water cooled copper conductor with a cross section area of 0.53 cm^2 and total length of 500 m. The magnet operates at a maximum of 400 A to provide up to 1.5 kG at photocathode. Fig:6 shows the magnetic field map of the cathode solenoid. Here, the solenoid field was distorted at the end due to the steel casing of the focusing solenoids next to it.

The beamline downstream of the gun solenoid consists of two fluorescent YAG screen-slit combinations at 1.5 m and 2.0 m and one YAG screen harp combination at 3.75 m. The YAG screens and slits were used to measure the transverse density profile and to trace the beam rotation angles. Additionally, in order to focus and steer the beam to the end of the beamline, four focusing solenoids and nine correctors were used.

5 Measurements

In order to measure how space charge effect varies with the magnetization, we increased the laser power at the cathode while keeping the other parameters constant and measured the average current at the end of the beamline for different solenoid strengths (0, 100, 200 A). We used focusing solenoids and correctors to make sure the beam transported cleanly throughout the beamline to the dump. According to the QE equation,

$$QE = \frac{hc}{\lambda e} \frac{I}{P} \times 100\% = \frac{124}{\lambda} \frac{I}{P} \%, \quad (18)$$

where P (W) is the incident laser power, I (mA) is the measured average current, λ is the laser wavelength (515 nm), h is Planck's constant (6.626×10^{-34} Js), e is the electron charge (1.602×10^{-19} C), and c is the speed of light (2.998×10^8 m/s). From this equation, we can relate the incident power to the extracted charge for a fixed QE value ($I_{\text{avg}} = Q_{\text{extracted}} f$).

According to equations (11) and (12) space charge effect is proportional to the applied voltage and inversely proportional to the bunch dimensions. Thus, we varied the laser spot size at the cathode (1.54, 1.0, 0.5, and 0.251 mm), laser pulse width (120, 70, 1 ps) and gun voltages (200, 150, 100 kV) and followed the same procedure for the magnetized and non-magnetized beam.

6 Results and Discussion

Below are the results of above experiment. Fig:7 shows the variation of extracted charge with the laser pulse energy and thus, according to the incident laser power and measured averaged current, how QE varies (18) for different magnetization strengths.

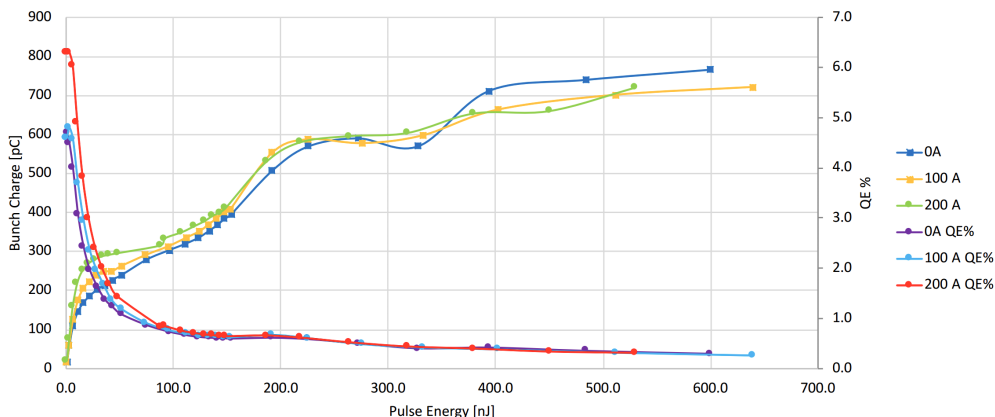


Figure 7: Bunch charge vs laser pulse energy and corresponding QE for different solenoid currents

Here, bunch energy is used as the independent variable by normalizing the laser power for the laser repetition rate. According to our results space charge limitations were initiated around 0.3 nC and increased for a maximum of 0.7 nC. We believe that charge extracted from 0.3 nC to 0.7 nC are come from the edges of the Gaussian beam. The actual bunch charge corresponding to the maximum laser energy, without taking into account the space charge is roughly 14 nC. This indicate that the beam is scraping , thus the beam pipe size and strength of the focusing solenoids are not enough to transport a clean beam to the dump. The wiggle behavior in high bunch charge region can be also a result of this beam loses. Moreover, QE also shows inversely proportional trend to the charge extracted, which is also a result of the space charge limitations. Note that at the beginning of QE plots, two different values are shown, as we switched the photocathodes in between. The higher QE was gained from the molybdenum substrate. Moreover, up to 100 nJ there is a significant effect of magnetization on the space charge limitations. Higher mignetization extracted more charge by mitigating the space charge effect. But later it didn't follow the same trend.

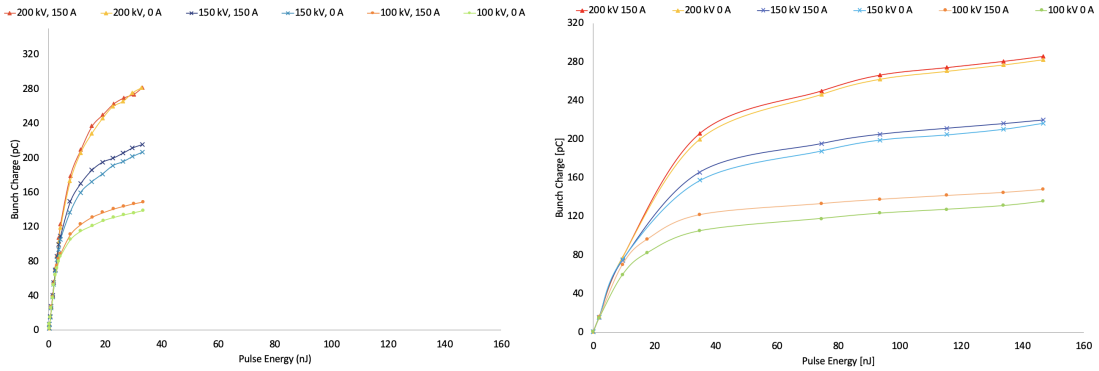


Figure 8: Bunch charge vs laser pulse energy variation with different gun voltages for magnetized and non-magnetized beam; 120 ps (Left), 1ps (Right)

Fig:8 shows how the space charge limitation varies with the gun HVs for magnetized and non magnetized beam for 120 ps and 1 ps pulse lengths. These plots roughly follow the idea of Child's law as gun HV increases, extracted charge should also increase. Also, by comparing the two plots, we can see that the long pulse length beam meets the space charge limit later than the short pulse length beam, which again follows the space charge force equation (11). However, in all of these cases there is little dependence on the magnetization. Note that, by the time we took this set of data, laser was not functioning well at high power range. Thus, we were unable to reach the maximum power, as shown in Fig:7.

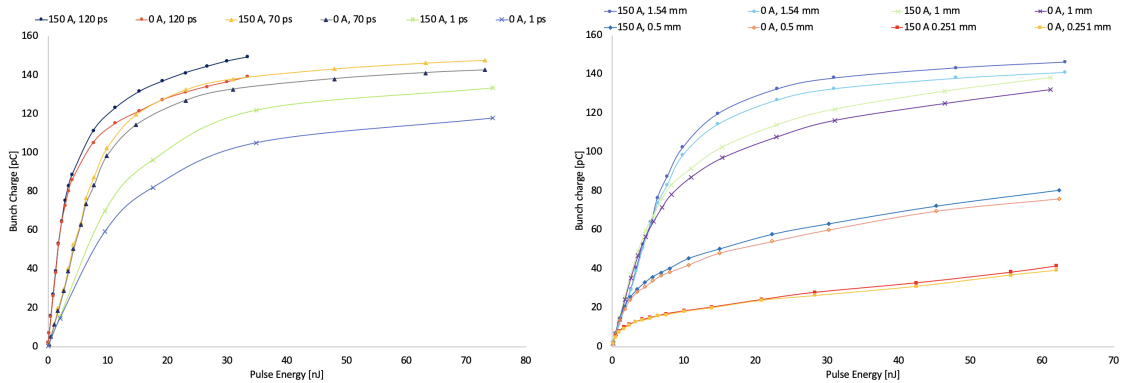


Figure 9: Bunch charge vs laser pulse energy variation with bunch length for magnetized and non-magnetized beam (Left). Bunch charge vs laser pulse energy variation with laser spot size for magnetized and non-magnetized beam(Right).

Fig:9 shows the space charge limitations varies with the pulse length for a fixed gun HV and space charge limitations varies with the laser spot size at the cathode in both magnetized and non magnetized cases. Again, both agree with the space charge force equation: by increasing the bunch dimensions, space charge forces can be suppressed leading to an increase in the extracted charge. However, both show little dependence on the magnetization.

7 Simulations

Two different simulation codes, GPT (General Particle Tracer) and ASTRA (A Space Charge Tracking Algorithm) have been used to model the beam line and reproduce the measurements [12, 13]. GPT is capable of modelling the 2D and 3D space charge situations, which is an advantage for non-symmetric beam simulations, and ASTRA is capable of 2D space charge simulations.

So far GPT simulations have been done by varying the bunch charge of the beam from pC to few nC and tracking the extracted charge from the cathode up to 1 m with highest accuracy possible. The 3D electric field map of the gun from CST Microwave Studio and the 2D magnetic field map of the gun solenoid from Opera were used and scaled for 225 kV gun HV and different solenoid currents respectively. Following table shows the other simulation parameters used.

Table 1: Simulation parameters

Mean transverse energy	0.130 eV
Transverse beam profile	Gaussian
Beam size (rms)	1.54×10^{-3} m
Temporal beam profile	Gaussian
Bunch length (FWHM)	75 ps
Beam pipe radius	3.6×10^{-2} m
Y off set	1.7×10^{-3} m
Number of particles	5000

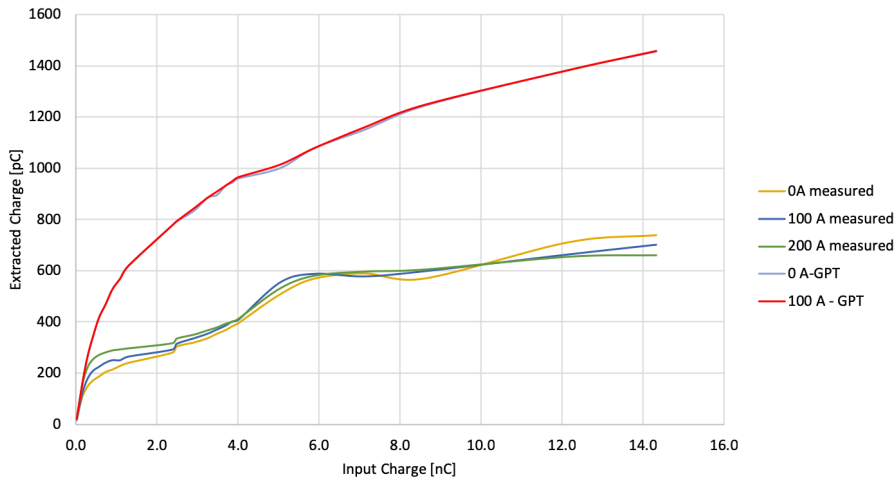


Figure 10: Comparison between measurements and simulations for extracted charge vs input charge.

Fig:10 shows the comparison between the measurements and simulations, which I have been done so far and it shows that in simulations space charge limitations start much later than the measured value. Note that, in simulations, only the space charge effect near the cathode (1 m from photocathode) was considered, not the beam transport part up to 4 m. Hence, there can be some discrepancies at higher laser energies due to beam losses, but at lower laser energies (0-2 nC input

bunch charge range), simulations should match the measurements. Moreover, simulations shows no dependence of magnetization on space charge current limitations.

8 Summary

In summary, we used Jefferson Lab's magnetized electron beam to investigate the space charge effect in magnetized beam. A new laser source was installed at GTS specifically for this experiment which was capable of delivering nC bunch charge (high power and varying repetition rate up to 50 kHz) with low average current. Measurements were taken by varying the laser power and tracking the average current at the end of the beam line for different magnetization strengths. We repeated this measurements for different gun HV, laser spot sizes and laser pulse widths. Our results showed that the space charge forces are inversely proportional to the beam dimensions and proportional to the gun voltage in agreement with equations (11) and (12). They also show a little dependence of magnetization on space charge current limitations. Furthermore, simulations that were carried out so far are not consistent with the measurements.

My future work will involve more simulations on this topic using both GPT and ASTRA programs and try to identify the mismatch in measurements and simulations. In addition, more beam based measurements will be planned with new laser, molybdenum substrate with smaller active area etc.

References

- [1] W. Herr and B. Muratori. *Concept of Luminosity*. Yellow Report CERN 2006-002.
- [2] G. I. Budker. *Atomnaya Energiya*, 22(346), 1967.
- [3] Y. Derbenev. *Theory of electron cooling*. 1978.
- [4] Ya. Derbenev and A. Skrinsky. Magnetization effect in electron cooling. *Sov. J. Plasma Phys*, 4:492, 1978.
- [5] M. Reiser. *Theory and Design of Charged Particle Beams*. 2008.
- [6] K.-J. Kim N. Barov S. Lidia J. Santucci R. Tikhoplav J. Wennerberg Y.-E Sun, P. Piot. Generation of angular-momentum-dominated electron beams from a photoinjector. *Phys. Rev. ST Accel. Beams*, 7, 2004.
- [7] M.A. Mamun et al. Production of magnetized electron beam from a dc high voltage photogun. *Proceedings of IPAC2018, Vancouver, Canada*, 2018.
- [8] M. Migliorati M. Ferrario and L. Palumbo. Space charge effects. *Proceedings of the CAS-CERN Accelerator School, Geneva*, 2014.
- [9] I. Langmuir. The effect of space charge and residual gases on thermionic currents in high vacuum. *Phys. Rev.* 2, pages 450–486, 1913.
- [10] J. P. Verboncoeur Y. Feng. Transition from fowler-nordheim field emission to space charge limited current density. *Phys. Plasmas* 13., 2006.
- [11] Ya. Derbenev. A method to overcome space charge at injection. *AIP Conf. Proc.*, 2005.
- [12] M.J. de Loos S.B. van der Geer. *General Particle Tracer User manual*.
- [13] K.Flöttmann. *A Space charge Tracking Algorithm online user manual*
http://www.desy.de/~mpyflo/Astra_dokumentation.